



Multi-Particle Model for a Commercial Blended Lithium-Ion Electrode

Z. Mao, M. Farkhondeh,* M. Pritzker,**,z M. Fowler, and Z. Chen

Department of Chemical Engineering, University of Waterloo, Waterloo, Ontario N2L 3G1, Canada

A mathematical model is presented to describe the electrochemical performance of a $\text{LiNi}_{1/3}\text{Mn}_{1/3}\text{Co}_{1/3}\text{O}_2$ – LiMn_2O_4 (NMC-LMO) blended cathode obtained from a commercial lithium-ion battery. The model accounts for the multiple particle sizes of the active materials in terms of three distributions: one for LMO particles, one for NMC primary and one for NMC secondary particles which likely are agglomerates of primary particles. The good match between the simulated and experimental galvanostatic discharge and differential-capacity curves supports the assumption that the secondary particles are nonporous under conditions where currents of 2C and below are applied. A thermodynamically consistent equation for diffusive flux is used to describe transport across the active particles. The corresponding thermodynamic factors are estimated from the equilibrium potentials of the active materials present in the electrode, while the particle size distribution and effective electronic conductivities of each component have been directly measured. Since the model is able to accurately describe the utilization of the various particle sizes and determine the contribution of each component at different discharge rates, it can serve as a useful tool for customizing the designs and predicting the discharge profiles of electrode blends made up of different active materials having a range of particle sizes.

© 2015 The Electrochemical Society. [DOI: 10.1149/2.0321603jes] All rights reserved.

Manuscript submitted September 29, 2015; revised manuscript received November 19, 2015. Published December 18, 2015.

Research and development of lithium-ion batteries (LIBs) has been underway for several decades. Numerous successive technical breakthroughs have enabled them to become more and more commercially viable for applications ranging from portable electronics to power tools. However, for automotive applications, LIBs face particular materials and engineering challenges: both their energy and power requirements have to be met simultaneously while slowing their aging so that vehicle lifespan is commercially viable. Some success in meeting these challenges has been achieved by loading battery electrodes with two or more active materials. Each of the active materials contributes at least one of the required characteristic properties of the blended electrode systems.¹ Examples of such blended systems are layered-layered mixtures of $\text{LiNi}_x\text{Co}_y\text{Al}_{1-x-y}\text{O}_2$ – LiCoO_2 (NCA-LCO),² layered-spinel mixtures of $\text{LiNi}_x\text{Co}_y\text{Al}_{1-x-y}\text{O}_2$ – LiMn_2O_4 (NCA-LMO),^{3,4} $\text{LiNi}_x\text{Mn}_y\text{Co}_{1-x-y}\text{O}_2$ – LiMn_2O_4 (NMC-LMO),⁵ layered-olivine mixtures of LiCoO_2 – LiFePO_4 (LCO-LFP)⁶ and spinel-olivine mixtures of LiMn_2O_4 – LiFePO_4 (LMO-LFP).⁷

Porous composite electrodes are at the heart of LIBs and their properties and manufacturing methods are of crucial importance. The main steps for the preparation of LIB electrodes include active-material selection, material synthesis and electrode manufacturing (formulation and fabrication). Properties such as the active particle size distribution (PSD) are particularly important when optimizing the performance of an electrode since they directly determine the power capability of the electrode. Electrode manufacturing, on the other hand, contributes to the electrode microstructure. More specifically, additives and fillers should be well dispersed and undergo little or no particle clustering or agglomeration. This will ensure a uniform porosity distribution across the electrode and less tortuous ionic and electronic pathways reaching the active particles. Overall, the fabrication of electrode should contribute to maximizing and stabilizing battery capacity, lifetime and rate capability.

The active material PSD has been shown to affect the electrochemical performance of LIB electrodes.^{8–12} These studies have provided theoretical bases for some phenomena associated with the particle-size distribution, such as poor coulombic efficiency and longer open-circuit relaxation time of an electrode with a non-uniform PSD compared to the one with a uniform PSD,⁹ rate-dependent dynamics of LiFePO_4 electrodes,^{8,12} the effect of particle size on lithium deposition when a LIB becomes overcharged¹⁰ and the influence of non-uniform size distribution on the electrode packing density.¹¹

Optimal design and operation of blended cathode systems benefits from physics-based mathematical models which can describe

the response of the electrode to various charge/discharge pulses. Few mathematical models for blended cathodes have been reported in the literature. Albertus et al. used a physics-based model to simulate the electrochemical behavior of NCA-LMO blended electrodes at various compositions. Their model which featured a distribution of resistances among the electrode particles (i.e., in line with the resistive reactant model^{8,13–14}) and was able to satisfactorily fit experimental data.³ Jung et al. compared simulation results to experimental galvanostatic discharge data from graphite-soft carbon/NMC-LMO full cells at various anode and cathode compositions.⁵

In our previous work,¹⁵ a simple mathematical model was developed to estimate the composition of an unknown commercial blended cathode by simulating galvanostatic discharge under a low-rate condition. This approach combining experimental data from X-ray powder diffraction and differential-capacity analysis with a mathematical model was shown to successfully characterize the unknown blended electrode (NMC-LMO) and accurately estimate its composition (in that case a 7:3 mass ratio). The model presented in the current communication is intended for a different purpose. It is more comprehensive and accounts for porous electrode effects and the particle-size distribution of the active materials in the previously identified NMC-LMO blended cathode. The model is suitable for a wide range of rate conditions from C/25 to 2C. Simulations are compared with experimentally determined galvanostatic discharge and differential-capacity curves and used to determine the contribution of each cathode component to the capacity. Finally, the effect of particle size on the electrode rate capability is discussed.

Experimental

In this work, some physical and electrochemical parameters of a fresh and unused commercial NMC-LMO blended cathode such as thickness and the effective electronic conductivity were measured and then used to develop parameters for a mathematical model. To obtain its electrochemical performance, the same blended cathode was used to fabricate cathode|separator|Li coin cells. The procedure involved opening and disassembling a commercial pouch cell, taking out a cathode sheet (double-side-coated on aluminum current collector) and removing the electrode coating on one side of the sheet. This was done using N-methyl-2-pyrrolidone (NMP) solvent. Circular samples ($A = 1.013 \text{ cm}^2$) were then punched from the one-sided electrode for coin cell assembly. To remove any possible electrolyte salt deposit, the circular samples were washed and rinsed with dimethyl carbonate (DMC). The washed samples were examined by SEM (Zeiss ULTRA) to characterize their surface morphology and to measure the electrode thickness prior to being fabricated into coin cells. Li was used as

*Electrochemical Society Student Member.

**Electrochemical Society Active Member.

^zE-mail: pritzker@uwaterloo.ca

the reference/counter electrode in the coin cells. The electrodes were separated by Celgard 2500 soaked with an electrolyte containing 1 M LiPF₆ dissolved in a 1:1 EC/DMC solution. The entire cell fabrication process from the opening of the pouch cell to the washing of the samples in DMC and finally to the assembly of the coin cells was carried out in an argon-filled glove box.

A series of galvanostatic experiments was conducted on coin cells using a Neware CT-3008-5V10 mA-164-U battery cycler. Prior to these experiments, the cells were first subjected to a sequence of 5 formation cycles identical to the one used in our previous study¹⁵ to ensure that the coin cells had reached a stable state and behaved consistently and repeatably during the subsequent galvanostatic tests. The waveform during each of these 5 formation cycles was identical. It consisted of the following steps: i) charging at a constant rate of C/2 until a potential of 4.2 V was reached, ii) 60 min. rest period (i.e., zero current), iii) charging at a constant rate of C/100 until a potential of 4.2 V was reached, iv) 60 min. rest period, v) discharging at a constant rate of C/2 until a potential of 3.0 V was reached, vi) 60 min. rest period, vii) discharging at a constant rate of C/100 until a potential of 3.0 V was reached and viii) 60 min. rest period. Due to equipment limitations, galvanostatic experiments were conducted in the constant current- constant current (CC-CC) mode instead of constant current-constant voltage (CC-CV) mode. The second CC step (constant current) (steps iii and vii above) was conducted at a very small C-rate such as C/100 in order to ensure that the electrode was fully lithiated (delithiated) by the end of discharge (charge). This served the same function as the CV step when using the CC-CV mode.

Following these 5 formation cycles, a series of galvanostatic experiments was carried out, each of which consisted of the following steps: i) charging at a particular rate until a potential of 4.2 V was reached, ii) 3-hour rest period, iii) charging at C/100 until a potential of 4.2 V was reached, iv) 3-hour rest period, v) discharging at the same rate as step i) until a potential of 3.0 V was reached, vi) 3-hour rest period, vii) discharging at C/100 until a potential of 3.0 V was reached, iv) and 3-hour rest period. Currents applied during steps i) and v) of this series of experiments followed the sequence: C/25, C/10, C/5, C/2, 1C and 2C. 1C rate corresponds to 2mA applied current.

The effective electronic conductivity of the electrode was measured using a four-probe setup consisting of a probe fixture (probe head: C4S 67/1, Cascade microtech Inc.) and a source meter (Keithley 2440 5A Source Meter, Keithley Instruments Inc.). More details regarding this measurement procedure are given in Ref. 16. The electronic conductivity of the porous electrode was expected to be several orders of magnitude smaller than that of the aluminum current collector (~3.5 × 10⁷ S m⁻¹). Conductivity measurement of a 2-layer aluminum/porous electrode medium was therefore prone to a significant error because most of the applied current should flow through the aluminum layer and bypass the porous electrode, not to mention the influence of the contact resistance between the two layers on conduc-

tivity measurements. To avoid such unnecessary errors, the aluminum current collector was dissolved by dipping the samples in a 1 M NaOH solution for a very short period of time (1–3 minutes). The electrode was then rinsed with DI water to remove the remainder of the solute as well as the reaction products and dried on a glass slide at room temperature. Care was taken not to damage the delaminated electrode.

Mathematical Model Development

A previously developed pseudo-two dimensional (P2D) electrochemical model¹⁷ is adapted here to account for particles having a different chemical nature and a non-uniform size distribution as shown in Figure 1. The model is used to simulate the rate capability of NMC-LMO blended cathodes and is validated against experimental data. The charge/discharge process involves phenomena occurring on the particle-scale and electrode-scale which are included in the model. At the particle-scale, lithiation/delithiation within each particle is controlled by solid-state diffusion of lithium ions that is coupled with charge-transfer reactions at the surface. The porous-electrode theory of Newman and co-workers¹⁸ is applied to describe electrode-scale transport within the cathode domain. It is assumed that the blended electrode consists of spherical particles that are distinguished in terms of their active material type n and size class m defined by their radii $R_{n,m}$. N total types of active material are present and the range of particles radii is discretized into M total size classes. Furthermore, any single particle consists of only one type of active material. The transport equation and associated boundary conditions describing the diffusion of Li ions within each particle of radius $R_{n,m}$ are given by Eqs. 1–3 below:

$$\frac{\partial c_{n,m}}{\partial t} = \frac{1}{r^2} \frac{\partial}{\partial r} \left(D_{n,m} r^2 \frac{\partial c_{n,m}}{\partial r} \right) \quad [1]$$

$$\left. \frac{\partial c_{n,m}}{\partial r} \right|_{r=0} = 0 \quad [2]$$

$$\left. \frac{\partial c_{n,m}}{\partial r} \right|_{r=R_{n,m}} = -\frac{i_{n,m}}{F D_{n,m}} \quad [3]$$

where $c_{n,m}$ is the intercalated Li concentration in the active material n with the particle size class m , $i_{n,m}$ is the current density on the surface of active material n with the particle size class m , r is the radial distance from the center of the particle, t is time and F is the Faraday constant. $D_{n,m}$ is the chemical diffusion coefficient for the intercalated species within active material n with the particle size class m and is related to the thermodynamic factor $\alpha_{n,m}$ and binary diffusion coefficient \mathcal{D}_n , as given in Eqs. 4–5 below:^{8,12,19}

$$D_{n,m} = \alpha_{n,m} \mathcal{D}_n \quad [4]$$

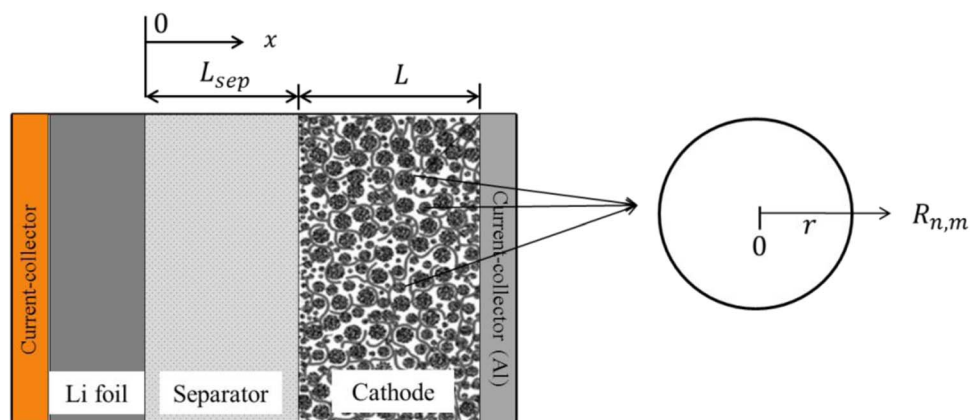


Figure 1. Schematic diagram of the porous half-cell containing a blended cathode for which a multi-particle pseudo-two-dimensional model is developed.

$$\alpha_{n,m} = -\frac{F}{RT} y_{n,m} (1 - y_{n,m}) \frac{\partial U_{n,m}}{\partial y_{n,m}} \quad [5]$$

Active materials are considered to be non-ideal solid solutions with the non-idealities manifested by their thermodynamic factors. The derivation of the above expression for the thermodynamic factor from the equilibrium potential can be found in detail in Refs. 8 and 12. In Eqs. 4 and 5, $y_{n,m}$ is the normalized lithium concentration in active material n with the particle size class m calculated from the ratio of the lithium concentration $c_{n,m}$ at any point along the particle radius to the maximum concentration c_n^{max} , i.e., $y_{n,m} = c_{n,m}/c_n^{max}$. The current density $i_{n,m}$ is related to the exchange current density $i_{n,m}^0$ and overpotential $\eta_{n,m}$ on the surface of active material n with the particle size class m by the Butler-Volmer equation:

$$i_{n,m} = i_{n,m}^0 \left[\exp\left(\frac{(1-\beta_n)F}{RT} \eta_{n,m}\right) - \exp\left(-\frac{\beta_n F}{RT} \eta_{n,m}\right) \right] \quad [6]$$

where,

$$i_{n,m}^0 = F k_n (c_e)^{(1-\beta_n)} (c_{s,n,m})^{\beta_n} (c_n^{max} - c_{s,n,m})^{\beta_n} \quad [7]$$

$$\eta_{n,m} = \Phi_1 - \Phi_2 - U_{n,m}(y_{n,m}) \quad [8]$$

$c_{s,n,m}$, $U_{n,m}(y_{n,m})$, k_n and β_n are the surface concentration, equilibrium potential, rate constant and transfer coefficient, respectively, associated with the charge-transfer reaction on the surface of active material n with the particle size class m . Φ_1 is the potential of the solid-phase (conductive matrix) and Φ_2 is the potential of the liquid-phase (electrolyte) in immediate contact with the active materials along the electrode thickness. Finally, c_e , T and R are the electrolyte concentration, temperature and gas constant, respectively. The governing equations describing the system at the electrode level are listed in Table I.

The charge balance across the conductive matrix of the porous electrode can be expressed as the sum of the electronic current densi-

ties entering/leaving all active material particles:¹⁸

$$\nabla \cdot \mathbf{i}_1 = -\xi \sum_{n=1}^N \sum_{m=1}^M \xi_{n,m} a_{n,m} i_{n,m} \quad [9]$$

where \mathbf{i}_1 is the electronic current density through the conductive matrix and obeys the electroneutrality condition with the liquid-phase current density \mathbf{i}_2 , i.e., $\nabla \cdot (\mathbf{i}_1 + \mathbf{i}_2) = 0$. ξ is the total volume fraction of all active materials in the entire electrode and can be calculated from the electrode capacity Q and active material capacity q_n . $a_{n,m}$ is the specific surface area and is calculated from the particle radius $R_{n,m}$, i.e., $a_{n,m} = 3/R_{n,m}$. $\xi_{n,m}$ is the volume fraction of particles composed of active material n with size m relative to the volume of all active materials and can be calculated from the density ρ_n and mass fraction $\xi'_{n,m}$ as follows:

$$\xi_{n,m} = \frac{\xi'_{n,m} / \rho_n}{\sum_{n=1}^N \left(\sum_{m=1}^M \xi'_{n,m} / \rho_n \right)} \quad [10]$$

subject to the condition,

$$\sum_{n=1}^N \sum_{m=1}^M \xi_{n,m} = 1 \quad [11]$$

The mass fraction of each active material is determined using the method described in detail in Ref. 15. The mass fraction of each particle size class in each active material is obtained by fitting the model to experimental discharge curves, as will be discussed in the next section.

All equations at the particle and electrode scales are coupled and solved simultaneously using the COMSOL Multiphysics 4.4 finite-element simulation package. The electrode and separator in the x -direction are each discretized into 10 intervals, while the particle domain is discretized into 20 elements in the r -direction. All equations are solved numerically until the stop condition corresponding to a cell voltage of 3.0 V on discharge is reached.

Table I. Electrode-level equations.

Solid-phase charge balance	Boundary conditions
$\mathbf{i}_1 = -\sigma_{\text{eff}} \nabla \Phi_1$ $\nabla \cdot \mathbf{i}_1 = -\xi \sum_{n=1}^N \sum_{m=1}^M \xi_{n,m} a_{n,m} i_{n,m}$ $\sum_{n=1}^N \sum_{m=1}^M \xi_{n,m} = 1$ $a_{n,m} = \frac{3}{R_{n,m}}$ $E = \Phi_1 _{x=L_{\text{sep}}+L} - \Phi_f$	$\mathbf{i}_1 = 0 \text{ at } x = L_{\text{sep}}$ $\mathbf{i}_1 = I/A \text{ at } x = L_{\text{sep}} + L$
Liquid-phase charge balance	
$\nabla \cdot \mathbf{i}_2 = 0$ $i_2 = -\kappa_{\text{eff,sep}} \nabla \Phi_2 + \frac{2\kappa_{\text{eff,sep}} RT(1-t_+^0)}{F c_e} \left(1 + \frac{d \ln f_{\pm}}{d \ln c_e} \right) \nabla c_e$ $\kappa_{\text{eff,sep}} = \kappa \epsilon_{\text{sep}}^y$ $\nabla \cdot (\mathbf{i}_1 + \mathbf{i}_2) = 0$ $i_2 = -\kappa_{\text{eff,cat}} \nabla \Phi_2 + \frac{2\kappa_{\text{eff,cat}} RT(1-t_+^0)}{F c_e} \left(1 + \frac{d \ln f_{\pm}}{d \ln c_e} \right) \nabla c_e$ $\kappa_{\text{eff,cat}} = \kappa \epsilon_{\text{cat}}^y$	$\Phi_2 = 0 \text{ at } x = 0$ $i_2 _{\text{sep}} = i_2 _{\text{cat}} \text{ at } x = L_{\text{sep}}$ $i_2 _{\text{sep}} = i_2 _{\text{cat}} \text{ at } x = L_{\text{sep}}$ $i_2 = 0 \text{ at } x = L_{\text{sep}} + L$
Electrolyte mass balance	
$\epsilon_{\text{sep}} \frac{\partial c_e}{\partial t} = \nabla \cdot (\epsilon_{\text{sep}} D_{\text{eff,sep}} \nabla c_e) - \frac{i_2 \nabla t_+^0}{F}$ $D_{\text{eff,sep}} = D_e \epsilon_{\text{sep}}^{y-1}$ $\epsilon_{\text{cat}} \frac{\partial c_e}{\partial t} = \nabla \cdot (\epsilon_{\text{cat}} D_{\text{eff,cat}} \nabla c_e) - \frac{i_2 \nabla t_+^0}{F} + \frac{(1-t_+^0) \xi \sum_{n=1}^N \sum_{m=1}^M \xi_{n,m} a_{n,m} i_{n,m}}{F}$ $D_{\text{eff,cat}} = D_e \epsilon_{\text{cat}}^{y-1}$ $D_e = \frac{c_1}{c_0} \left(1 + \frac{d \ln f_{\pm}}{d \ln c_e} \right) \mathcal{D}_e$	$\epsilon_{\text{sep}} \frac{\partial c_e}{\partial x} = -\frac{I(1-t_+^0)}{F D_{\text{eff,sep}} A} \text{ at } x = 0$ $\frac{\partial c_e}{\partial x} _{\text{sep}} = \frac{\partial c_e}{\partial x} _{\text{cat}} \text{ at } x = L_{\text{sep}}$ $\frac{\partial c_e}{\partial x} _{\text{sep}} = \frac{\partial c_e}{\partial x} _{\text{cat}} \text{ at } x = L_{\text{sep}}$ $\frac{\partial c_e}{\partial x} = 0 \text{ at } x = L_{\text{sep}} + L$
Lithium foil counter electrode kinetics	
$I = -A i_f^0 \left[\exp\left(\frac{(1-\beta_f)F}{RT} (\Phi_f - \Phi_2 _{x=0})\right) - \exp\left(-\frac{\beta_f F}{RT} (\Phi_f - \Phi_2 _{x=0})\right) \right]$	

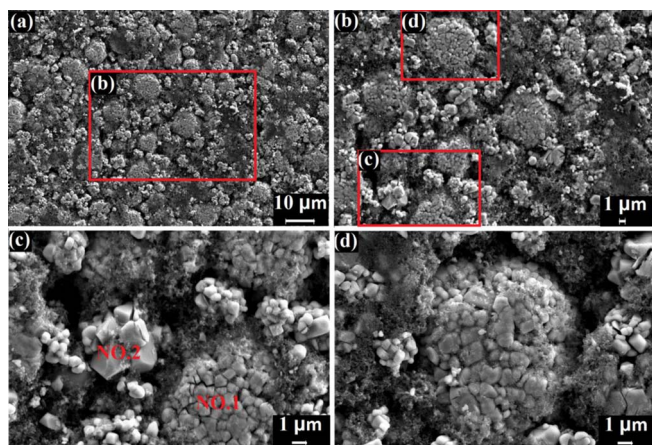


Figure 2. SEM images of NMC-LMO blended cathode surface obtained at different magnifications. Image in (a) is shown at 1000x. Highlighted region in (a) is shown at magnification 2000x in (b). Highlighted regions in (b) are shown at magnification 5000x in (c) and (d).

Results and Discussion

Surface morphology and particle size measurement.—SEM examination of the morphology of the electrode surface at 1000x and 2000x magnification in Figures 2a and 2b, respectively, reveals a structure that is relatively homogeneous, but made up of particles with a complex size distribution. Figure 2c shows an enlarged view of the area labelled as (c) in Figure 2b. It clearly reveals two types of particles that are labelled as NO.1 and NO.2. As described in detail previously,¹⁵ NO.1 corresponds to NMC particles which make up 70 wt% of the blended cathode and NO.2 to LMO particles that constitute the remaining 30 wt%. Analysis of the SEM images shows that the NMC particles have a very wide range of sizes, with the ratio of the size of the smallest particles to that of the largest particles being $\sim 1:10$. Previous SEM and EDX analysis of the morphology of the electrode surface shown in Figures 2c and 2d clearly revealed that the NMC particles lie within two distinctly different size distributions. The first group is made up of very small NMC particles with diameters smaller than $1 \mu\text{m}$, while the other group includes larger particles that are a few micrometers in diameter. Consequently, we distinguish between these two groups – the first termed as ‘primary’ or ‘submicron’ NMC particles and the second group as ‘secondary’ or ‘micron’ NMC particles. These secondary particles have presumably formed by the agglomeration/clustering of the primary particles. On the other hand, the size distribution of LMO particles is found to be much narrower than that of the NMC particles, with a ratio of the size of the smallest particles to that of the largest particles of $\sim 1:3$. The LMO particles for the most part are large with diameters of $1\text{--}3 \mu\text{m}$.

Based on these considerations, we sub-divide NMC particles into a submicron group and a micron group and fit a separate particle-size distribution for each portion. Due to the difficulty in experimentally separating the NMC and LMO particles from each other and using standard particle size measurement techniques on each group to obtain their size distributions, we determine their sizes directly from SEM images and take advantage of the fact that EDX analysis enables the NMC and LMO particles to be distinguished. The method we adopt is to analyze more than 300 NMC particles from several SEM images obtained at 5000x and 1000x magnification, measure their diameters from these images, separate them into submicron (smaller than $1 \mu\text{m}$) and micron (larger than $1 \mu\text{m}$) groups and fit functions to the size distributions of these two groups. Similarly, we measure the diameters of more than 300 LMO particles from several SEM images at 5000x magnification and fit a single function to their size distribution.

The cumulative PSDs of the three groups of active materials, i.e., submicron and micron groups for NMC and one group for LMO, measured from the SEM images are shown in Figure 3. In each of the three cases, a log-normal function is found to fit the experimental data very well. d_{50} values of $0.87 \mu\text{m}$ and $9.29 \mu\text{m}$ are obtained for the NMC submicron and micron groups, respectively, and $1.74 \mu\text{m}$ for the LMO particles.

Although the complete size distributions for the submicron and micron groups of NMC particles and micron group of LMO particles can be incorporated into Eqs. 1–3, this would greatly complicate the model. Before resorting to such a level of complexity, we adopt the simpler approach of assuming the particles in each of these groups have uniform size with a diameter given by the corresponding d_{50} . Thus, using the nomenclature presented above, N is set to 2 since the cathode contains two types of active materials NMC and LMO. NMC particles denoted with index $n = 1$ have two sizes ($M = 2$), while LMO particles denoted as $n = 2$ have only one size ($M = 1$). Based on their d_{50} sizes, the sizes of the NMC and LMO particles are as follows: $R_{1,1} = 0.435 \mu\text{m}$, $R_{1,2} = 4.65 \mu\text{m}$ and $R_{2,1} = 0.87 \mu\text{m}$ (see Table II).

According to the model proposed by Dargaville and Farrell,²¹ agglomerates constitute mesoscale porous particles composed of smaller primary particles and conductive additives with electrolyte filling in the pores. The charge-transfer reaction occurs at the surfaces of the smaller particles wherever both electron and reacting ion are present. In brief, porous-electrode theory can be applied to the secondary particles. However, it adds a great deal more complexity to our model which is already quite complex and makes the estimation of the parameters associated with the agglomerate considerably more difficult. Therefore, for our purposes, we consider the agglomerate to be a nonporous particle in which solid-state diffusion is the only transport mechanism. With this assumption, we have been able to obtain excellent fits of the model to the experimental data, as will be shown later, and obtain reasonable parameter estimates.

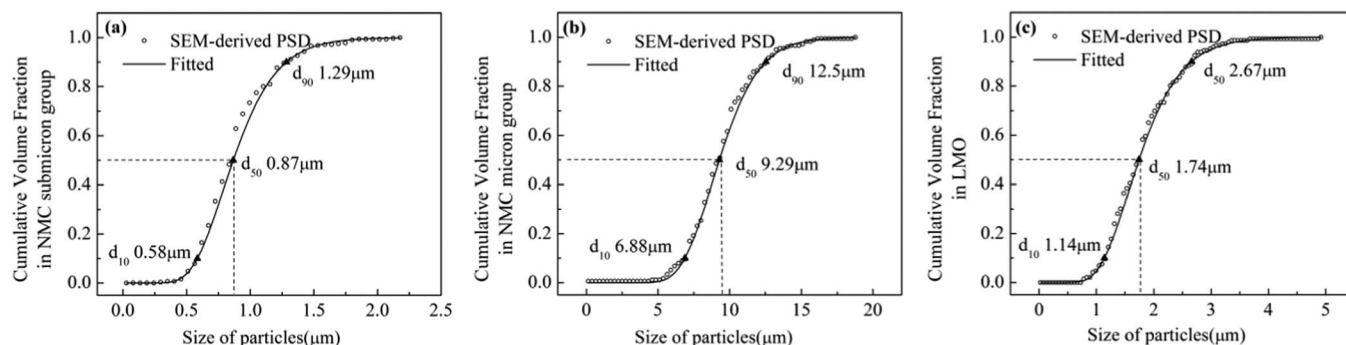


Figure 3. Measured (symbols) and fitted (solid line) particle size distributions for (a) NMC submicron group, (b) NMC micron group and (c) LMO. d_{10} , d_{50} and d_{90} values are marked in each case.

Table II. List of model parameters.

Parameter	Symbol	LMO	NMC
Cathode area (m ²)	<i>A</i>	0.0001013 ^m	
Electrode thickness (m)	<i>L</i>	5.7 × 10 ⁻⁵ m	
Cathode capacity (Ah)	<i>Q</i>	0.002 ^m	
Total active-material volume fraction	ξ	0.558 ¹⁵	
Solid-state thermodynamic factor	α _{<i>n,m</i>}	Eq. 5	
Radius of type <i>n</i> particle in size class <i>m</i> (m)	<i>R</i> _{<i>n,m</i>}	8.7 × 10 ⁻⁷ m	4.65 × 10 ⁻⁶ m (micron group) 4.35 × 10 ⁻⁷ m (submicron group)
Capacity of type <i>n</i> particle (Ah kg ⁻¹)	<i>q</i> _{<i>n</i>}	100 ³	151 ²⁰
Maximum lithium concentration in type <i>n</i> particle (mol m ⁻³)	<i>c</i> _{<i>n</i>} ^{max}	23339 ³	49761 ²⁰
Density of type <i>n</i> particle (kg m ⁻³)	ρ _{<i>n</i>}	4220 ^a	4770 ^a
Charge-transfer coefficient for charge transfer on type <i>n</i> cathode particle	β _{<i>n</i>}	0.5 ^a	0.5 ^a
Electrode porosity	ε _{cat}	0.35 ^a	
Initial electrolyte concentration (mol m ⁻³)	<i>c</i> _{<i>e</i>}	1000 ^m	
Separator thickness (m)	<i>L</i> _{sep}	2.5 × 10 ⁻⁵ Celgard	
Lithium ions transference number	<i>t</i> ₊ ⁰	0.36 ^a	
Bulk diffusion coefficient in the electrolyte (m ² s ⁻¹)	<i>D</i> _{<i>e</i>}	5.2 × 10 ⁻¹⁰ 8	
Bulk ionic conductivity of the electrolyte (S m ⁻¹)	κ	1.3 ⁸	
Charge-transfer coefficient for charge transfer on Li foil electrode	β _{<i>f</i>}	0.5 ^a	
Separator porosity	ε _{sep}	0.37 ^{Celgard}	
Bruggeman exponent	γ	1.5 ^a	
Effective electronic conductivity (S m ⁻¹)	σ _{eff}	9.65 ^m	
Exchange current density on Li foil electrode (A m ⁻²)	<i>i</i> _{<i>f</i>} ⁰	20 ^a	
Faraday constant (C mol ⁻¹)	<i>F</i>	96485	
Gas constant (J mol ⁻¹ K ⁻¹)	<i>R</i>	8.314	
Temperature (K)	<i>T</i>	298	

^mmeasured^{Celgard}Celgard product data sheet^aassumed based on literature

Equilibrium-potential functions.—The equilibrium potentials for lithiation/delithiation of NMC and LMO have been obtained from references 20 and 3, respectively. For both materials, C/25 galvanostatic charge/discharge conditions are slow enough for the resulting potential-stoichiometry curves to reflect suitable equilibrium potentials over the potential window of 3.0–4.2V. In the current study, we assume that the equilibrium potential of each active material is the average of the charge and discharge curves at any given degree of lithiation obtained at the rate of C/25.

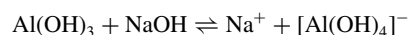
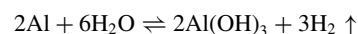
The stability window of the electrolyte used for the cell assembly determines the upper and lower cutoff potentials of any battery active material. With the active materials and the electrolyte used here, the potential window of 3.0 – 4.2 V vs. Li/Li⁺ guarantees the stability of the two active materials as well as the electrolyte. The theoretical capacity of NMC is 277Ah kg⁻¹ while its usable capacity is about 151Ah kg⁻¹ (the remaining unused capacity of 126Ah kg⁻¹ is used to protect the crystal structure from damage due to excessive charging beyond 4.2 V).²⁰ Therefore, the initial value of *y*_{*n,m*} for NMC particles in the blended cathode during discharge (final value during charging), which corresponds to the minimum lithium content, is taken to be (277-151)/277 = 0.45. The same analysis holds true for LMO where *y*_{*n,m*} = 0.35 for LMO particles at a potential of 4.2V and so *y*_{*n,m*} = 0.35 is taken to be the initial value for this component of the blended cathode. Both the simulations and experiments are conducted until *y*_{*n,m*} = 1.0 (i.e., assumed to coincide with the lower cutoff potential of 3.0 V) in both types of particles during discharge. Based on the above consideration, two functions previously proposed in Refs. 22 and 23 are fitted separately to the experimental equilibrium potentials of NMC and LMO to yield Eqs. 12 and 13, respectively:

$$U_{\text{NMC}}(y_{\text{NMC}}) = 6.51176 - 8y_{\text{NMC}} + 7.1086y_{\text{NMC}}^2 - 1.55y_{\text{NMC}}^3 - 0.459y_{\text{NMC}}^6 - 5.00034 \times 10^8 \exp(135.089y_{\text{NMC}}^2 - 118.089) \quad [12]$$

$$U_{\text{LMO}}(y_{\text{LMO}}) = 0.225 - 0.392y_{\text{LMO}} + 2.2 \tanh[-1010(y_{\text{LMO}} - 0.994)] + 1.9 \tanh[-21.4(y_{\text{LMO}} - 1.04)] + 0.181 \operatorname{sech}[23.4(y_{\text{LMO}} - 0.397)] - 0.175 \operatorname{sech}[24.2(y_{\text{LMO}} - 0.399)] + 0.0164 \operatorname{sech}[13.1(y_{\text{LMO}} - 0.567)] + 0.33 \operatorname{sech}[48.1(y_{\text{LMO}} - 1)] \quad [13]$$

Effective electronic conductivity

The effective electronic conductivity of the electrode has been measured using a four-probe setup. Prior to this conductivity measurement, the samples are treated by soaking in a 1M NaOH solution for few minutes at ambient temperature. Rapid delamination of the electrode is observed due principally to hydrogen bubbling at the interface between the porous electrode and the aluminum current collector. Hydrogen evolution occurs due to the fast Al dissolution in the presence of sodium hydroxide according to the following chemical reactions:



It has been shown in previous studies that the PVDF binder^{24–26} and conductive additive^{27–28} are not damaged and that the electrode active materials NMC^{29–30} and LMO³¹ are not corroded under the conditions applied during this process.

The 4-point probe setup consists of four equally spaced metal tips with finite radius making contact with the test subject along a line. The electric current is carried through the two outer probes and the voltage is recorded across the inner two probes. Valdes³² considered seven different measurement cases and provided formulas and correction divi-

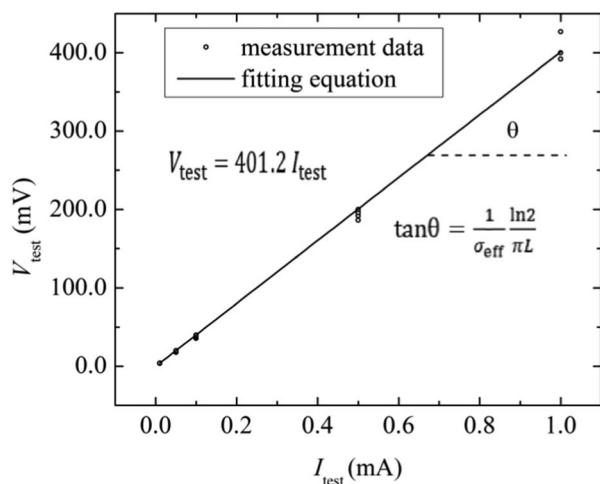


Figure 4. The measurement of effective electronic conductivity of the electrode.

sors to compute the resistivity based on geometrical considerations for each one. The samples in this study fall into case 7 analyzed by Valdes (after removal of the aluminum collector). Accordingly, the equation used to determine the effective electronic conductivity is given as:

$$V_{\text{test}} = \frac{1}{\sigma_{\text{eff}}} \left(\frac{\ln 2}{\pi L} \right) I_{\text{test}} \quad [14]$$

where I_{test} , V_{test} and L are the applied current, measured potential difference and electrode thickness, respectively. Once the voltage response to various applied currents is determined (Figure 4), the effective electronic conductivity is calculated by fitting Eq. 14 to the data. It should also be noted that the applied current is small enough not to burn the porous electrode. The estimated value of the effective electronic conductivity (9.65 S m^{-1}) is within the range of previously reported conductivity values of porous battery electrodes using a multi-probe method developed in Ref. 33.

The dimensional analysis of Ohm's law applied to porous electrodes reported in Ref. 19 yields the following simple equation for Φ_1 across the x -axis in a porous electrode:

$$\Phi_1 = \frac{IL}{\sigma_{\text{eff}}} \left(\frac{x^2}{2} - \frac{1}{6} \right) + \Phi_1^{\text{avg}} \quad [15]$$

where Φ_1^{avg} is the average solid-phase potential. Given that the parameters L and σ_{eff} have values of $57 \times 10^{-6} \text{ m}$ and $= 9.65 \text{ S m}^{-1}$, respectively, the order of the first term is $O(10^{-6}I)$, while the second term Φ_1^{avg} is of order $O(1)$. Therefore, only at extremely high

currents is the solid-phase potential non-uniform given the uniform conductive filler dispersion and the effective conductivity estimated earlier. In other words, the value of such a large effective electronic conductivity has no significant impact on the electrode potential over the operating conditions of interest to this research. The effect of the electrode formulation and its microstructure on the effective conductivity is beyond the scope of this paper and will not be discussed here. The model parameters either measured or obtained from the literature are listed in Table II.

Fitting of model to experimental potential-capacity curves.—

The six remaining model parameters with unknown values are the rate constants for charge transfer k_1 of NMC and k_2 of LMO, binary diffusion coefficient \mathcal{D}_1 of Li in NMC particles and binary diffusion coefficient \mathcal{D}_2 of Li in LMO particles and the mass fractions $\xi'_{1,1}$ and $\xi'_{1,2}$ of NMC particles in the submicron and micron groups, respectively, relative to the total mass of active material. Since the total mass fraction of NMC particles in both the submicron and micron groups is already known from our previous study to be 0.7, $\xi'_{1,1}$ and $\xi'_{1,2}$ are no longer independent of each other, i.e., $\xi'_{1,1} + \xi'_{1,2} = 0.7$. The five parameters are then adjusted to fit the model presented in the previous section to the complete set of experimental potential-capacity curves obtained at the rates C/25, C/10, C/5, C/2, 1C and 2C. The results are shown in Figure 5. Table III presents the values of k_1 , k_2 , \mathcal{D}_1 , \mathcal{D}_2 , $\xi'_{1,1}$ and $\xi'_{1,2}$ so obtained by this fitting procedure. As shown in Figure 5a, the agreement between the model-fitted and experimental curves is very good at all currents. A small discrepancy is observed at potentials close to 3.6V. This can be explained by the fact that the NMC equilibrium potential in the model is assumed to be the average value between the potentials obtained during a low-rate discharge and a low-rate charge at each Li stoichiometry, as detailed before, and the hysteresis between the discharge and charge curves is largest at this potential.

The dependence of the end-of-discharge capacity on the current for the NMC-LMO (70:30 wt%) blended cathode as determined experimentally and from the model is presented in Figure 5b. The capacities plotted in this case are obtained from Figure 5a and correspond to the values when the cell is in its discharged state at the lower cutoff potential of 3.0 V. Again, the model-fitted curve agrees very well with the experimental curve.

The values we have obtained for the rate constants k_1 and k_2 of the two active materials lie within the range of those previously reported in the literature.^{3,15,22,34} In the sensitivity analysis described in the next section, the effects of decreasing and increasing these rate constants by one order of magnitude, i.e., from 3×10^{-12} to 5×10^{-10} will be discussed. From the knowledge of the binary diffusion coefficients for Li (Table III) and the dependence of the equilibrium potential $U_{n,m}$ on $y_{n,m}$, both the NMC and LMO chemical diffusion coefficients can be calculated using Eqs. 4 and 5 as functions of the

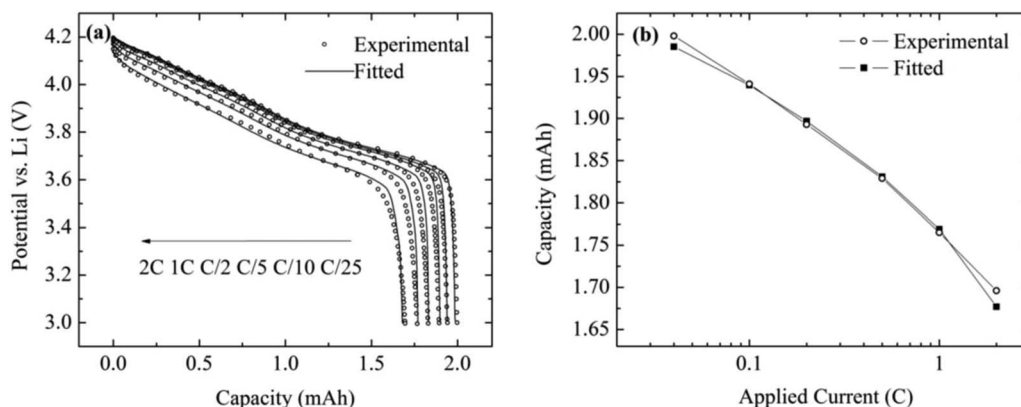


Figure 5. Comparison of the experimental and model-fitted (a) potential-capacity curves and (b) end-of-discharge capacity-current curves for discharge of a blended cathode with NMC: LMO composition of 0.7:0.3 by mass.

Table III. List of model parameters.

Parameter	Symbol	LMO	NMC
Rate constant for charge transfer on type n cathode particle (mol/[m ² s(mol m ⁻³) ^{1.5}])	k_n	3×10^{-11f}	3×10^{-11f}
Binary diffusion coefficient of Li in type n particle (m ² s ⁻¹)	D_n	1.0×10^{-16f}	1.1×10^{-16f}
Mass fraction of type n particle among total active materials	$\xi'_{n,m}$	0.3 ¹⁵	0.22 ^f (micron group) 0.48 ^f (submicron group)

^ffitted in the current study to the experimental potential-capacity data.

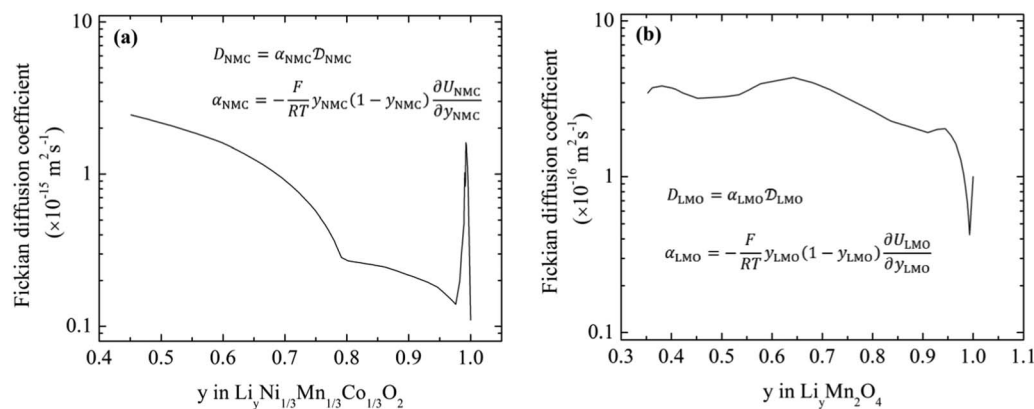
local lithium concentration within active particles. A similar approach has been reported previously for other chemistries.^{8,12,19,35–38} The resulting values of the diffusion coefficients presented in Figure 6 vary from $\sim 10^{-16}$ to $\sim 10^{-15}$ m²s⁻¹ and from $\sim 10^{-17}$ to $\sim 10^{-16}$ m²s⁻¹ for NMC and LMO, respectively, and are well within the range of those reported previously for these active materials by characterizing single-component electrodes. For instance, values in the ranges 10^{-16} to 10^{-14} (model)²⁰ and 10^{-18} to 10^{-17} m²s⁻¹ (PITT)³⁹ were obtained for NMC and LMO, respectively. However, other values, such as 3.9×10^{-21} to 2.4×10^{-17} for NMC (EIS)⁴⁰ and 10^{-17} to 10^{-12} (CV, PSCA, EIS and model)^{41–48} for LMO, were found depending on the particle size, crystal defects in the samples and the measurement techniques used. A noteworthy feature of both plots in Figure 6 is the sharp spike in the dependence of diffusion coefficient on lithium content at values of y close to 1 which can be attributed to the steep drop in equilibrium potential that occurs at these stoichiometries.

The differential-capacity curve is an intrinsic electrochemical signature for each active cathode material and so provides a good means for analyzing the contributions of each component to the electrode response over the course of lithiation or delithiation. In our previous work, the normalized differential capacity was used to successfully identify the active components in a blended cathode by matching the positions of three peaks for the same blended cathode, i.e., ~ 3.75 V, ~ 4.00 V and ~ 4.14 V, with those obtained for single-component NMC and LMO cathodes (see Figure 2 of Ref. 15). The results showed that the first peak is associated with NMC, while the other two peaks are attributed to LMO. A comparison of the experimental and simulated differential-capacity curves is presented in Figure 7. The determination of the differential-capacity curves essentially entails the numerical estimation of the tangents at many points along the potential-capacity curves. Consequently, the values so obtained are very sensitive to small changes and subtle details of the potential-capacity curves. A comparison of the experimental and computed curves in Figure 7 shows good agreement at all rates, most notably with regard to the peak positions. The good agreement between the measured and simulated curves gives confidence that the multi-particle model is able to accurately capture the contributions of NMC and LMO to the overall response at different rates.

The differential-capacity curves from C/25 to 2C exhibit either three (C/25, C/10, C/5 and C/2) or two (1C and 2C) peaks, reflecting that both NMC and LMO contribute to the discharge behavior at all rates. The peak positions in the differential-capacity curves continually shift toward lower potential as the C-rate increases. This trend is understandable given that the potential at any capacity during the discharge process would be expected to decrease (i.e., increase in overpotential) when the C-rate is raised (Figure 5a). In addition, the NMC signature peak appearing at the lowest potential decreases in magnitude, whereas the LMO signature peak at an intermediate potential increases in magnitude as the C-rate increases. At the same time, the other peak at high potential associated with LMO gradually shrinks and finally disappears altogether when the current reaches 2C.

The contributions of the total current and capacity of the blended cathode due to the LMO component at charge rates of C/25 and 2C over the course of the discharge, as computed according to the model, are presented in Figures 8a and 8b. Two maxima in the LMO contribution appear during the initial stages of discharge at low C-rate (Figure 8a). However, at high C-rate, only a single maximum in the current contribution of LMO is observed (Figure 8b), which coincides with the disappearance of one of the LMO differential-capacity peaks. The LMO component always contributes the higher proportion of the total current in the blended NMC-LMO cathode during the first half of discharge. The peak in the differential-capacity curves associated with LMO which occurs at higher potential (Figure 7) contributes more to the discharge current early in the overall cell discharge (Figures 8a and 8b) at lower rates (e.g., C/25) than at higher rates (e.g., 2C). As shown in Figures 8a and 8b, the LMO particles are completely lithiated by the time the cell approaches the midpoint of the discharge process whereupon their contribution to the overall current sharply drops to zero.

Once the LMO capacity has been consumed, NMC begins to fully dominate the discharge current of the blended cathode. Throughout the second half of the discharge process, virtually all of the current involves the NMC particles. An inflection point is observed in the capacity contribution curves for NMC at both C/25 and 2C (Figures 8c and 8d) and coincides with the point where the LMO particles become largely spent.

**Figure 6.** Calculated chemical diffusion coefficient of Li as a function of Li content during discharge of the single component (a) NMC and (b) LMO cathodes.

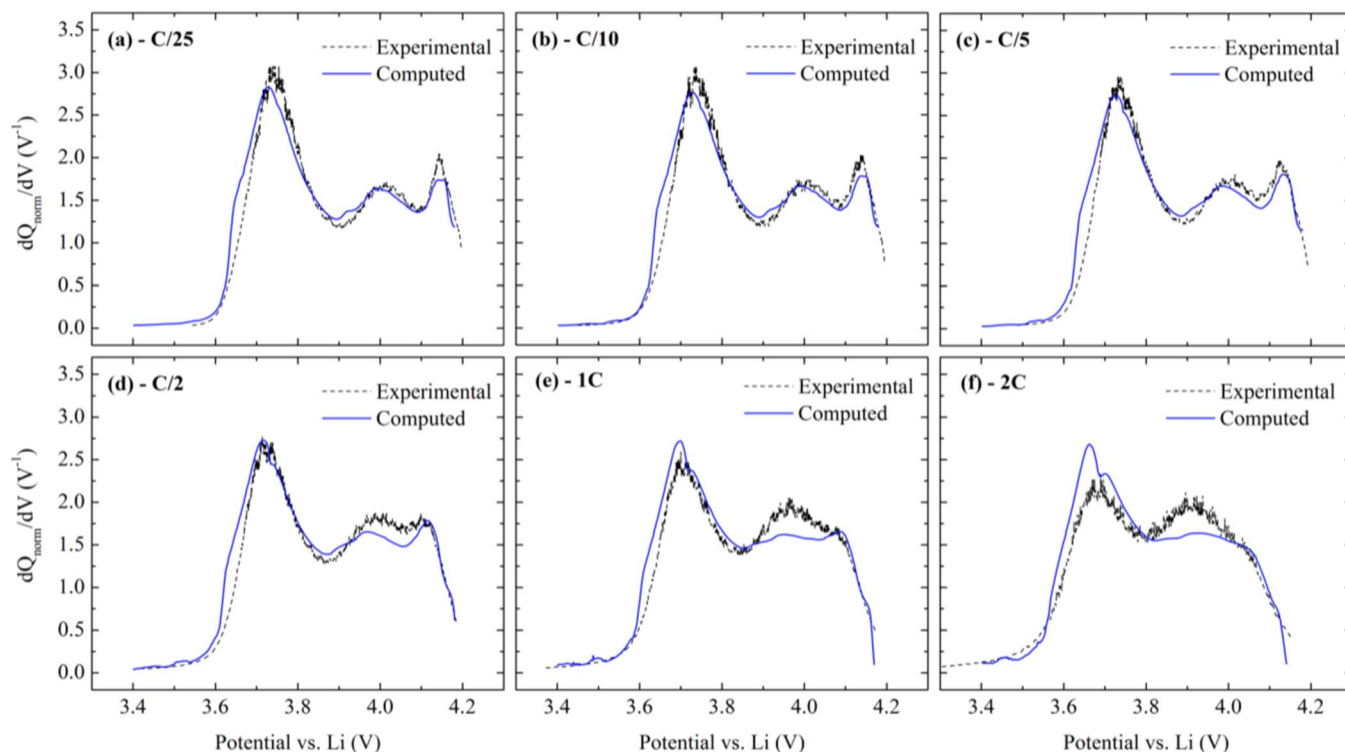


Figure 7. Experimental and computed differential-capacity curves of the NMC-LMO blended electrode at a C-rate of (a) C/25 (b) C/10 (c) C/5 (d) C/2 (e) 1C and (f) 2C.

Sensitivity analysis.—The sensitivity of the 5 fitted parameters reported in Table III and the effective electronic conductivity has been investigated by adjusting one parameter at the time while holding the others constant at their values listed in Tables II and III. The results are shown in Figure 9. As stated previously, the effect of decreasing and increasing the rate constants k_1 and k_2 of the two active materials by one order of magnitude on the discharge curves has been investigated. These rate constants have almost no significant impact on the

discharge curves at low C-rates (e.g., C/5); however, at high C-rates (e.g., 2C), the rate constant associated with NMC lithiation significantly affects the electrode potential and shifts the corresponding differential capacity peak toward lower potentials when it is decreased by one order of magnitude (Figure 9a). The rate constant of LMO lithiation affects the high-potential region of the potential-capacity curve and causes the associated peak in the differential capacity-potential curve to almost disappear when it is decreased by one order

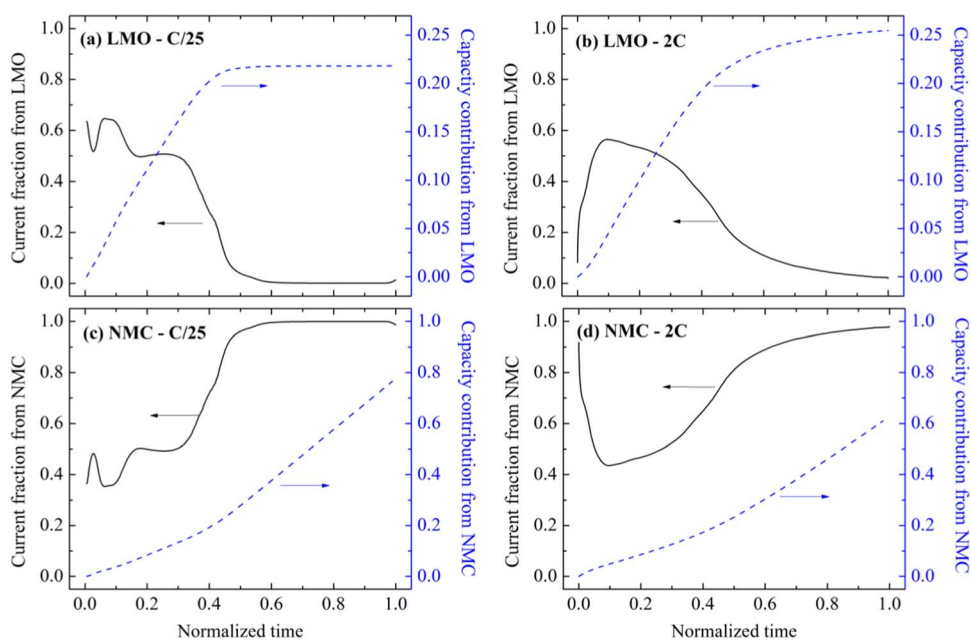


Figure 8. Variation in the total current and capacity of the blended cathode due to the LMO and NMC components with normalized time (i.e., with respect to the moment when simulations reach the lower cutoff potential of 3.0 V on discharge) over the course of a single discharge at rates of C/25 and 2C, i.e. (a) LMO-C/25 (b) LMO-2C (c) NMC-C/25 and (d) NMC-2C.

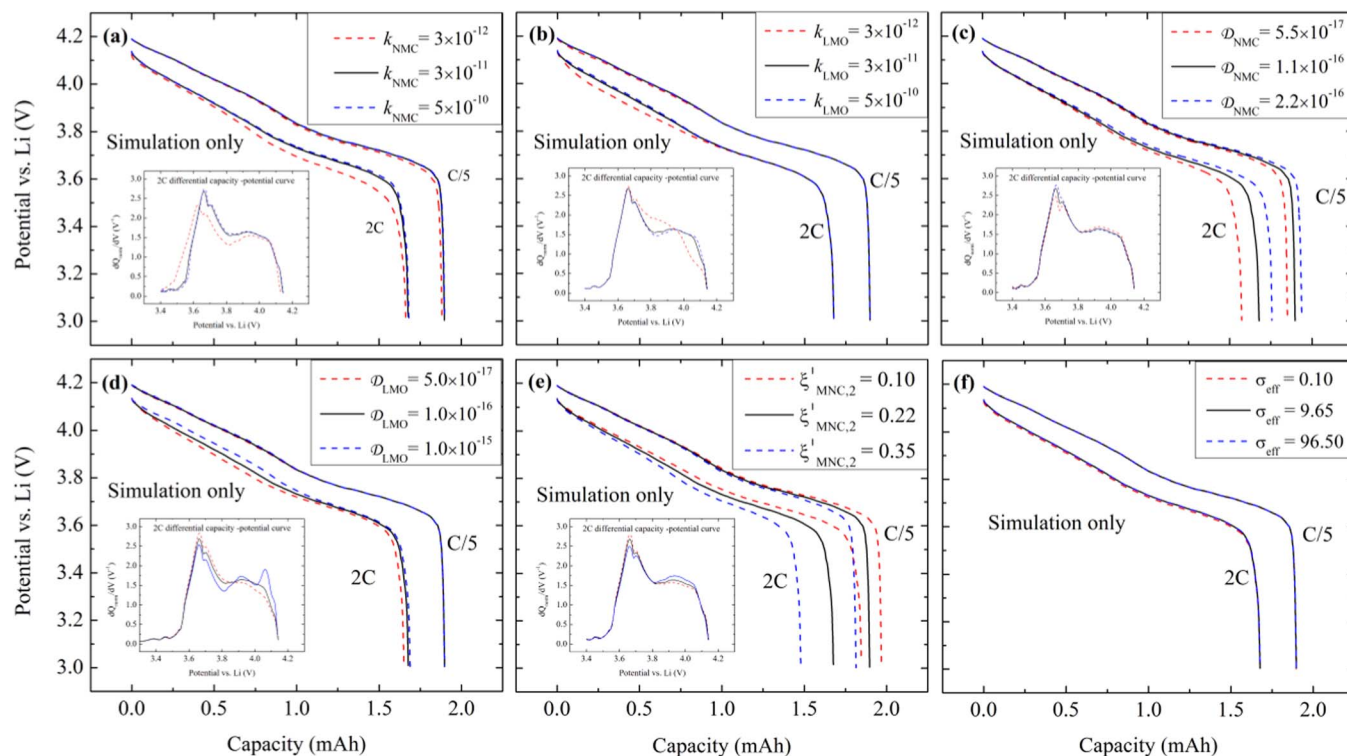


Figure 9. Multi-particle model sensitivity to (a) k_1 ($\text{mol} [\text{m}^2\text{s}(\text{mol m}^{-3})^{1.5}]^{-1}$) (b) k_2 ($\text{mol} [\text{m}^2\text{s}(\text{mol m}^{-3})^{1.5}]^{-1}$) (c) \mathcal{D}_1 (m^2s^{-1}) (d) \mathcal{D}_2 (m^2s^{-1}) (e) $\xi_{\text{NMC},2}^1$ and (f) σ_{eff} (S m^{-1}) at discharge rate of C/5 and 2C. 2C differential-capacity curves are shown in inset.

of magnitude (Figure 9b). The binary diffusion coefficient of NMC has a significant impact on the end-of-discharge capacity at both low and high C-rates; however, it does not affect the signature shape of the discharge curves as the differential-capacity curve remains almost unchanged regardless of the NMC binary diffusivity (Figure 9c). On the other hand, the binary diffusion coefficient of LMO has almost no impact on the end-of-discharge capacity regardless of the applied current but affects the high-potential differential-capacity peaks at 2C; the larger the diffusivity the greater the peak intensities (Figure 9d). The end-of-discharge capacity is very sensitive to the size distribution of NMC particles (i.e., $\xi_{\text{NMC},2}^1$) both at low and at high applied currents (Figure 9e), while the differential-capacity curve is not affected by changes in the NMC particle-size distribution. Finally the effective electronic conductivity is not a sensitive parameter at least for the operating currents of this study (Figure 9f), which is expected according to the dimensional analysis discussed earlier.

Overall, based on the sensitivity analyses of the 6 parameters, it is concluded that solid-state diffusion within NMC (i.e., both diffusion coefficient and particle-size distribution of the micron group) is the main limiting phenomenon during the discharge process. This is not surprising given that NMC contributes 70 wt% to the overall active material loading, one-third of which is in the form of large agglomerates (see Table III).

Particle-size effect.—As discussed previously, the size of the NMC particles is best described in terms of two separate groups, the sub-micron group and the micron group, with distinct distributions. These two groups combine to yield the overall performance contribution due to NMC presented in Figures 8c and 8d. The breakdown of the contribution of NMC according to these two groups is plotted in Figure 10. The trends for the capacity contribution during discharge are similar for both groups; however, the submicron particles contribute

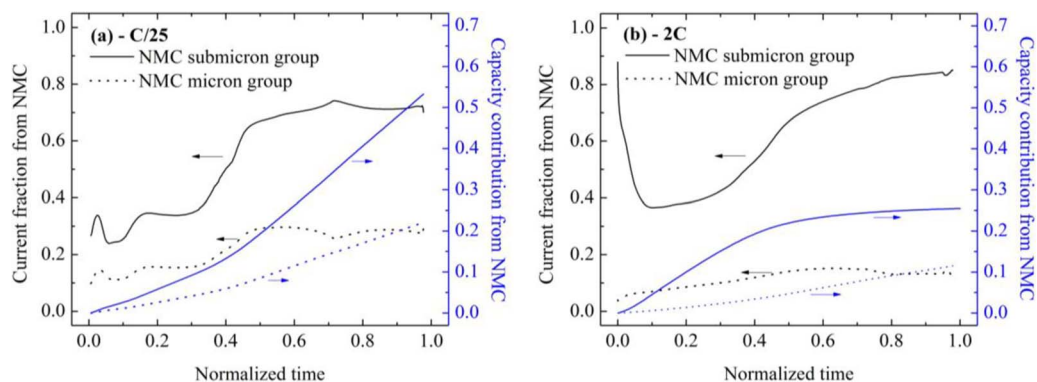


Figure 10. Variation of the fraction of the total current and capacity of the blended cathode due to the submicron and micron NMC groups with normalized time over the course of discharge at the rates of (a) C/25 and (b) 2C.

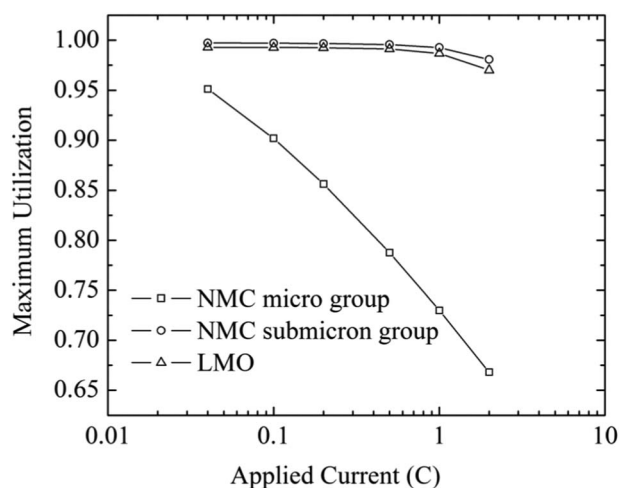


Figure 11. Effect of current on the maximum utilization of the LMO particles and the submicron and micron groups of NMC particles in the blended cathode.

much more to the current and capacity than do the micron particles. This result is not surprising since both diffusion and charge-transfer reaction limitations are smaller for the submicron particles than for the micron particles. Moreover, the cathode contains many more submicron NMC particles than micron particles (note their mass fractions in Table III).

The utilization of active particles is defined as the ratio of the amount of lithium within the spherical particles⁸ to the maximum amount based on c_n^{max} and can be calculated according to Eq. 16:

$$\begin{aligned} \text{Utilization} &= \frac{\int 4\pi r^2 c_{n,m} dr}{c_n^{max} \frac{4\pi R_{n,m}^3}{3}} = 3 \int \left(\frac{c_{n,m}}{c_n^{max}} \right) \left(\frac{r}{R_{n,m}} \right)^2 d \left(\frac{r}{R_{n,m}} \right) \\ &= 3 \int y_{n,m} (r/R_{n,m})^2 d (r/R_{n,m}) \end{aligned} \quad [16]$$

The value at the end of discharge is called the maximum utilization. A similar trend is evident upon examination of the effect of current on the maximum utilization of the LMO particles and the two groups of NMC particles as computed by the model and presented in Figure 11. The maximum utilization of the micron NMC particles drops from 0.95 to 0.65 with an increase in the discharge rate from C/25 to 2C. On the other hand, the maximum utilizations of both the LMO and submicron NMC particles remain above 0.97 at all C-rates, indicating that they contribute fully to the current and capacity until the lower cutoff potential is reached. The overall effect of the three classes of particles is that the total capacity of the blended cathode decreases as the discharge rate rises. Since the LMO and submicron NMC particles are considerably smaller than the micron NMC particles, these simulations once again emphasize that the size of NMC particles is a key factor affecting the total end-of-discharge capacity of the blended cathode.

To further investigate the effect of particle size, we use the model to compute the effect of current on the normalized end-of-discharge capacity of blended NMC: LMO cathodes with 70:30 wt% composition as determined at a potential of 3.0 V for the cases where the NMC particles are submicron only, micron only and submicron-micron mixtures obtained by end-of-discharge capacity as shows in Figure 5b (current case). As shown in Figure 12, if all NMC particles have the same submicron radius of 0.435 μm , the cathode achieves the highest capacity at any C-rate due to its greater utilization. For example, at the highest C-rate of 2C, the capacity reaches a level approximately 15% higher than that attained if the NMC component is made up of a mixture of submicron-micron particles. However, if all NMC particles are in the micron group and have a radius of 4.65 μm , the NMC utilization and the cathode capacity are dramatically lower;

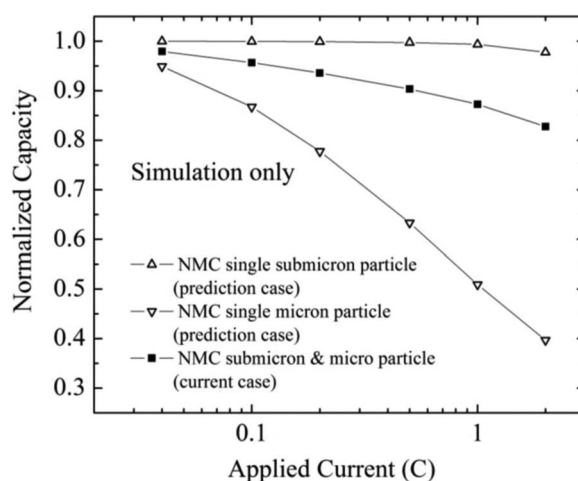


Figure 12. Effect of current on normalized capacity for electrodes composed of blended NMC and LMO with 70:30 wt% composition for the cases where the NMC particles are submicron only, micron only and ‘mixed’ submicron-micron obtained by averaging according to the mass fraction of these two groups.

the capacity is 52% lower at a 2C charge rate than if all NMC particles are submicron.

On the basis of the analysis above, it appears that reducing the amount of micron-sized particles and increasing the amount of submicron-sized particles in blended cathodes can effectively improve the utilization of NMC and further increase the cathode capacity, especially for discharge at high C-rates. During the material synthesis, a small and uniform primary-particle size is required to achieve a high material utilization. In addition, electrode manufacturing technology must be optimized to reduce active material particle agglomeration and clustering. Formation of secondary particles reduces ionic (i.e., through electrolyte) and electronic (i.e., through conductive matrix) access to the active sites. If the liquid-phase ionic percolation to the interior active sites in a porous secondary particle of a given size becomes less facile than the solid-state diffusion in a hypothetical primary particle of the same size, then the latter dominates Li transport and the secondary particle behaves effectively as a large nonporous particle.^{11,49-53} Adequate fit of the model to the experimental data suggests that our assumption of nonporous secondary particles is reasonable and significantly reduces model complexity and computational cost. Future work could be to refine the model by considering the agglomerates to be porous and by accounting for ionic and electronic losses across the porous secondary particles. To be of practical value, such a complex model should be able to accurately estimate agglomerate parameters such as porosity and effective conductivity.

Conclusions

A mathematical model has been implemented to describe the performance of a blended lithium-ion electrode. The model features particles with different sizes and chemical composition. More specifically, the electrode is loaded with two different active materials NMC and LMO. Since NMC forms agglomerates, it is sub-divided into 2 classes of particles, i.e., primary particles and secondary particles. The secondary particles are considered to be large non-porous NMC agglomerates. PSDs for the LMO particles, NMC primary and NMC secondary particles were obtained from SEM micrographs with the resulting d_{50} s used in the model. Expressions describing the dependence of the equilibrium potentials of NMC and LMO on the lithium concentration were fitted assuming that they can be obtained from the average of the potentials measured during charge and discharge at the low rate of C/25, similar to the procedure adopted by previous researchers.^{3,20} The effective electronic conductivity of the active materials was measured using a 4-point probe setup and its impact on

the electrode potential estimated by dimensional analysis of Ohm's law. The model also features variable solid-state diffusivity and treats the transport of intercalated species across active material particles in a thermodynamically consistent manner. The model has been shown to accurately capture the galvanostatic discharge data as well as the differential-capacity curves obtained from a blended NMC (70 wt%): LMO (30 wt%) cathode at various C-rates. This indicates that the assumption of nonporous secondary particles is reasonable at least over the operating condition of interest here, i.e., up to 2C applied current. This significantly simplifies the model and relaxes the need for characterizing the actual porous particles.

An important aspect of the model is that it enables the contribution of the respective particle sizes of each component over the course of the discharge to be evaluated at different C-rates. A sensitivity analysis of the fitted model parameters including kinetic rate constants and solid-state diffusivities has also been carried out. Finally, the utilization of the LMO particles and primary and secondary NMC particles over the range of applied currents has also been determined. For these reasons, this model can serve as a useful tool in the selection of the most appropriate active materials in electrode blends with multiple particle sizes and can also be used to customize electrode designs to obtain targeted discharge profiles.

Acknowledgment

The authors acknowledge the support of the General Motors Co., Automotive Partnership Canada (Project APCPJ 395996-09) and the Natural Sciences and Engineering Research Council of Canada (Project RGPIN-170912).

List of Symbols

A	cathode area (m^2)
$a_{n,m}$	specific surface area of active material n with particle size class m (m^{-1})
$c_{n,m}$	Li ion concentration in active material n with particle size class m (mol m^{-3})
c_e	Li ion concentration in electrolyte (mol m^{-3})
c_T	total Li ion concentration in electrolyte (mol m^{-3})
c_n^{max}	maximum concentration of Li within active material n (mol m^{-3})
D_n	solid-phase binary diffusion coefficient in active material n ($\text{m}^2 \text{s}^{-1}$)
D_e	diffusion coefficient of electrolyte based on a thermodynamic driving force, ($\text{m}^2 \text{s}^{-1}$)
$D_{n,m}$	Li ion solid-phase diffusion coefficient in active material n with particle size class m ($\text{m}^2 \text{s}^{-1}$)
$D_{\text{eff,sep}}$	effective diffusion coefficient of electrolyte in separator ($\text{m}^2 \text{s}^{-1}$)
$D_{\text{eff,cat}}$	effective diffusion coefficient of electrolyte in cathode ($\text{m}^2 \text{s}^{-1}$)
D_e	bulk diffusion coefficient in the electrolyte ($\text{m}^2 \text{s}^{-1}$)
E	cell potential (V)
F	Faraday constant (96480 C mol^{-1})
f_{\pm}	mean molar activity coefficient of inorganic salt in electrolyte
I	applied current (A)
$i_{n,m}^0$	exchange current density for lithiation/delithiation on active material n with particle size class m (A m^{-2})
i_1	solid-phase current density (A m^{-2})
i_2	liquid-phase current density (A m^{-2})
$i_{n,m}$	faradaic current density on active material n with particle size class m (A m^{-2})
i_f^0	exchange current density for charge transfer reaction on Li foil (A m^{-2})
k_n	rate constant ($\text{mol m}^{-2} \text{s}^{-1} (\text{mol m}^{-3})^{-3/2}$)
L	electrode thickness (m)
L_{sep}	separator thickness (m)

Q	cathode capacity (Ah)
q_n	practical capacity of type n particle (Ah kg^{-1})
$R_{n,m}$	particle radius of active material n with size class m (m)
R	gas constant ($8.314 \text{ J mol}^{-1} \text{K}^{-1}$)
r	radial distance within a particle of active material (m)
T	absolute temperature (K)
t	time (s)
t_+^0	lithium ion transference number
$U_{n,m}$	equilibrium potential for lithiation/delithiation on active material n with particle size class m (V)
$y_{n,m}$	lithium content in active material n with particle size class m

Greek

$\alpha_{n,m}$	solid-state thermodynamic factor of active material n with particle size class m
β_n	charge-transfer coefficient for lithiation/delithiation on active material n
β_f	charge-transfer coefficient for charge transfer reaction at lithium foil electrode
γ	Bruggeman exponent
ξ	total volume fraction of all cathode active material in the electrode
$\xi_{n,m}$	volume fraction of active material n with particle size class m
$\xi'_{n,m}$	mass fraction of active material n with particle size class m
ϵ_{cat}	porosity of cathode
ϵ_{sep}	porosity of separator
$\eta_{n,m}$	surface overpotential on active material n with particle size class m (V)
κ	electrolyte ionic conductivity (S m^{-1})
$\kappa_{\text{eff,cat}}$	effective ionic conductivity in blended electrode (S m^{-1})
ρ_n	density of type n particle (kg m^{-3})
σ_{eff}	effective electronic conductivity in blended electrode (S m^{-1})
Φ_1	solid-phase potential of cathode (V)
Φ_2	liquid-phase potential of electrolyte (V)
Φ_f	electrode potential of Li counter electrode (V)

Subscripts

n	active material type (NMC and LMO)
m	particle size class
avg	average value
cat	cathode
eff	effective
sep	separator
sur	surface
test	test data

References

- S. B. Chikkannavar, D. M. Bernardi, and L. Liu, *J. Power Sources*, **248**, 91 (2014).
- J. P. Schmidt, H. Y. Tran, J. Richter, E. Ivers-Tiffée, and M. Wohlfahrt-Mehrens, *J. Power Sources*, **239**, 696 (2013).
- P. Albertus, J. Christensen, and J. Newman, *J. Electrochem. Soc.*, **156**, A606 (2009).
- Y. L. Dai, L. Cai, and R. E. White, *J. Power Sources*, **247**, 365 (2014).
- S. Jung, *J. Power Sources*, **264**, 184 (2014).
- H. S. Kim, M. Kong, K. Kim, I. J. Kim, and H. B. Gu, *J. Electroceramics*, **23**, 219 (2008).
- C. Qiu, L. Liu, F. Du, X. Yang, C. Wang, G. Chen, and Y. Wei, *Chem. Res. Chinese Univ.*, **31**, 270 (2015).
- M. Farkhondeh, M. Safari, M. Pritzker, M. Fowler, T. Han, J. Wang, and C. Delacourt, *J. Electrochem. Soc.*, **161**, A201 (2014).
- R. Darling and J. Newman, *J. Electrochem. Soc.*, **144**, 4201 (1997).
- P. Arora, M. Doyle, and R. E. White, *J. Electrochem. Soc.*, **146**, 3543 (1999).
- G. S. Nagarajan, J. W. Van Zee, and R. M. Spotnitz, *J. Electrochem. Soc.*, **145**, 771 (1998).
- M. Farkhondeh and C. Delacourt, *J. Electrochem. Soc.*, **159**, A177 (2012).

13. K. E. Thomas-Alyea, *ECS Transactions*, **16**(13), 155 (2008).
14. M. Safari and C. Delacourt, *J. Electrochem. Soc.*, **158**(2), A63 (2011).
15. Z. Mao, M. Farkhondeh, M. Pritzker, M. Fowler, Z. Chen, and M. Safari, *J. Electrochem. Soc.*, **162**, A716 (2015).
16. B. M. Amoli, S. Gumfekar, A. Hu, Y. N. Zhou, and B. Zhao, *J. Mater. Chem.*, **22**, 20048 (2012).
17. M. Doyle, T. F. Fuller, and J. Newman, *J. Electrochem. Soc.*, **140**, 1526 (1993).
18. J. Newman and K. E. Thomas-Alyea, *Electrochemical Systems*, 3rd ed., Wiley Hoboken, NJ (2004).
19. M. M. Majdabadi, S. Farhad, M. Farkhondeh, R. A. Fraser, and M. Fowler, *J. Power Sources*, **275**, 633 (2015).
20. S. L. Wu, W. Zhang, X. Song, A. K. Shukla, G. Liu, V. Battaglia, and V. Srinivasan, *J. Electrochem. Soc.*, **159**, A438 (2012).
21. S. Dargaville and T. W. Farrell, *J. Electrochem. Soc.*, **157**(7), 830 (2010).
22. S. G. Stewart, V. Srinivasan, and J. Newman, *J. Electrochem. Soc.*, **155**(9), A664 (2008).
23. M. Safari and C. Delacourt, *J. Electrochem. Soc.*, **158**(5), A562 (2011).
24. I. Mathieson, D. M. Brewis, I. Sutherland, and R. A. Cayless, *J. Adhes.*, **46**, 49 (1994).
25. D. M. Brewis, I. Mathieson, I. Sutherland, R. A. Cayless, and R. H. Dahm, *Int. J. Adhes. Adhes.*, **16**, 87 (1996).
26. Q. F. Liu, C. H. Lee, and H. Kim, *Sep. Sci. Technol.*, **45**, 1209 (2010).
27. J. D. Lee and H. J. Yoon, In meeting abstracts, *The Electrochemical Society*, **6**, 554 (2012).
28. I. Lombardi, M. Bestetti, C. Mazzocchia, P. L. Cavallotti, and U. Ducati, *Electrochem. Solid-State Lett.*, **7**, A115 (2004).
29. L. Liu, K. Sun, N. Zhang, and T. Yang, *J. Solid State Electrochem.*, **13**(9), 1381 (2009).
30. S. B. Jang, S. H. Kang, K. Amine, Y. C. Bae, and Y. K. Sun, (2005). *Electrochim. Acta*, **50**(20), 4168 (2005).
31. X. Liu, J. Wang, J. Zhang, and S. Yang, *J. Mater. Sci: Mater. Electron.*, **17**(11), 865 (2006).
32. L. B. Valdes, *Proceedings of the IRE*, **42**(2), 420 (1954).
33. M. Ender, A. Weber, and E. Ivers-Tiffée, *Electrochem. Comm.*, **34**, 130 (2013).
34. J. Christensen, V. Srinivasan, and J. Newman, *J. Electrochem. Soc.*, **153**, A560 (2006).
35. M. W. Verbrugge and B. J. Koch, *J. Electrochem. Soc.*, **143**, 600 (1996).
36. Q. Zhang, Q. Z. Guo, and R. E. White, *J. Electrochem. Soc.*, **153**, A301 (2006).
37. J. Christensen and J. Newman, *J. Solid State Electrochem.*, **10**, 293 (2006).
38. D. K. Karthikeyan, G. Sikha, and R. E. White, *J. Power Sources*, **185**, 1398 (2008).
39. D. Aurbach, M. D. Levi, E. Levi, H. Teller, B. Markovsky, G. Salitra, and L. Heider, *J. Electrochem. Soc.*, **145**, 3024 (1998).
40. L. Wang, J. Zhao, X. M. He, J. Gao, J. J. Li, C. Wan, C. Jiang, J. J., C. Wan, and C. Jiang, *Int. J. Electrochem. Sci.*, **7**, 345 (2012).
41. F. Cao and J. Prakash, *Electrochim. Acta*, **47**, 1607 (2002).
42. D. A. Totir, B. D. Cahan, and D. A. Scherson, *Electrochim. Acta*, **45**, 161 (1999).
43. M. Mohamedi, D. Takahashi, T. Uchiyama, T. Itoh, M. Nishizawa, and I. Uchida, *J. Power Sources*, **93**, 93 (2001).
44. M. Nishizawa, T. Uchiyama, K. Dokko, K. Yamada, T. Matsue, and I. Uchida, *Bull. Chem. Soc. Japan*, **71**, 2011 (1998).
45. E. Deiss, D. Haringer, P. Novak, and O. Haas, *Electrochim. Acta*, **46**, 4185 (2001).
46. K. Dokko, M. Nishizawa, M. Mohamedi, M. Umeda, I. Uchida, J. Akimoto, Y. Takahashi, Y. Gotoh, and S. Mizuta, *Electrochem. Solid-State Letters*, **4**, A151 (2001).
47. M. Mohamedi, D. Takahashi, T. Itoh, M. Umeda, and I. Uchida, *J. Electrochem. Soc.*, **149**, A19 (2002).
48. J. Barker, K. West, Y. Saidi, R. Pynenburg, B. Zachau-Christiansen, and R. Koksang, *J. Power Sources*, **54**, 475 (1995).
49. T. Drezen, N. H. Kwon, P. Bowen, I. Teerlinck, M. Isono, and I. Exnar, *I. J. Power Sources*, **174**(2), 949 (2007).
50. M. Wagemaker, W. J. Borghols, and F. M. Mulder, *J. Am. Chem. Soc.*, **129**(14), 4323 (2007).
51. S. P. Sheu, C. Y. Yao, J. M. Chen, and Y. C. Chiou, *J. Power Sources*, **68**(2), 533 (1997).
52. R. Cornut, D. Lepage, and S. B Schougaard, *J. Electrochem. Soc.*, **159**(6), A822 (2012).
53. R. E. Garcia, Y. M. Chiang, W. C. Carter, P. Limthongkul, and C. M. Bishop, *J. Electrochem. Soc.*, **152**(1), A255 (2005).